High Temperature Oxidation Study of Nano-Y_2O_3 Dispersed Ferritic Alloys Synthesized by Mechanical Alloying and Sintering

A. MEHARWAL, M. KUMAR, S.K. KARAK, J. DUTTA MAJUMDAR, and I. MANNA

This study concerns mechanism and kinetics of isothermal oxidation of four Fe-Cr-Al-Ti ferritic alloys in the range 700 °C to 900 °C for up to 50 hours in air. These four alloys with nominal compositions of 83.0Fe-13.5Cr-2.0Al-0.5Ti (alloy A), 79.0Fe-17.5Cr-2.0Al-0.5Ti (alloy B), 75.0Fe-21.5Cr-2.0Al-0.5Ti (alloy C), and 71.0Fe-25.5Cr-2.0Al-0.5Ti (alloy D) each with 1.0 wt pct nano-Y_2O_3 dispersion were synthesized by mechanical alloying and sintering at 1000 °C by hot isostatic pressing, high pressure sintering, hydrostatic extrusion and pulse plasma sintering techniques. A detailed characterization of the phase aggregate, microstructure and micro-composition of the oxide scale was carried out by X-ray diffraction, scanning electron microscopy and energy dispersive spectroscopy, respectively. Oxidation kinetics appear to follow a parabolic rate with an activation energy of 135 to 234 kJ/mol, which depend on alloy composition (*i.e.*, Cr content). Oxidation mostly occurred by counter-ionic diffusion of oxygen from air to the interior and cations (Cr^{+3} or Fe^{+3}) from the bulk toward the surface. Alloy D sintered by hot isostatic pressing offered the highest resistance to oxidation.

https://doi.org/10.1007/s11661-020-05918-7

I. INTRODUCTION

OXIDATION is a major source of degradation and failure of structural components exposed to elevated temperature in thermal power plants including atomic power stations. Thermal power plants operated at higher temperature with water cooled environment in the supercritical state improves the energy conversion and fuel utilization efficiency and reduces environmental pollution.[1] Oxide dispersion strengthened (ODS) high Cr ferritic matrix alloys are considered more appropriate structural components in advanced nuclear energy reactors including fast breeder reactors, ultra-supercritical thermal power plants and solid oxide fuel cells due to their higher resistance to oxidation and creep, better thermal conductivity and lower coefficient of thermal expansion.[2–5] Conventional ferritic steels are considered unsuitable in these applications because of their poor oxidation resistance and creep-rupture strength at the usual operating temperatures of these reactors (~650 °C). Carbide strengthening is not acceptable because of the possibility of selective leaching of carbon in sodium environment. Ferritic alloys with ultrafine/nanometric oxide dispersion are projected as suitable materials for liquid sodium cooled nuclear power plants up to a temperature of 650 °C to 670 °C as they possess adequate void swelling and creep resistance and very low carbon concentration to suppress formation of TiC.[2–6]

Mechanically alloyed ferritic steels with yttria (Y_2O_3) dispersion were found to register higher creep resistance than conventional ferritic or martensitic steel of identical base composition.[5–8] Furthermore, presence of yttria dispersion at grain boundaries is considered an effective strategy to reduce grain boundary diffusion and prevent internal oxidation of the bulk.[9,10] In the past, four ferritic steels with nominal compositions of 83.0 Fe-13.5Cr-2.0Al-0.5Ti (alloy A), 79.0Fe-17.5Cr-2.0Al-0.5Ti (alloy B), 75.0Fe-21.5Cr-2.0Al-0.5Ti (alloy C), and 71.0Fe-25.5Cr-2.0Al-0.5Ti (alloy D) alloys (all in wt pct) were synthesized by us using solid state processing route comprising mechanical alloying and sintering (at 1000 °C) by four competitive methods of hot isostatic pressing, high pressure sintering, hydrostatic extrusion and pulse plasma sintering, respectively.[11–15] These alloys recorded very attractive range of bulk mechanical strength under compression, indentation hardness, Young's modulus and wear resistance under optimum processing condition, which were superior to conventional ferritic steels. Among these alloys, alloy D with the highest Cr content (25.5 wt pct Cr) manifested the best combination of mechanical properties in terms of

---

A. MEHARWAL, M. KUMAR, S.K. KARAK, J. DUTTA MAJUMDAR and I. MANNA are with the Metallurgical & Materials Engineering Department, Indian Institute of Technology Kharagpur, Kharagpur, W.B. 721302, India. Contact e-mail: imanna@metal.iitkgp.ernet.in

Manuscript submitted July 5, 2019.

compressive strength, hardness and elastic modulus.[11–15] However, comprehensive assessment of the oxidation resistance and related mechanism of these alloys has not been conducted until now.

Thus, the present study aims to carry out accelerated isothermal oxidation of the above stated four ferritic alloys in dry air in the temperature range 700 °C to 900 °C, which is significantly higher than the typical operating temperature in supercritical (550 °C to 570 °C), ultra-supercritical (600 °C to 620 °C) or advanced ultra-supercritical (650 °C to 670 °C) power plants. Furthermore, the mechanism of oxidation has been investigated through a detailed characterization of the composition, microstructure and phase aggregate of the oxide scale.

II. EXPERIMENTAL PROCEDURES

This study concerns four Fe-Cr-Al-Ti alloys with nominal compositions (in wt pct) of 83.0Fe-13.5Cr-2.0Al-0.5Ti (alloy A), 79.0Fe-17.5Cr-2.0Al-0.5Ti (alloy B), 75.0Fe-21.5Cr-2.0Al-0.5Ti (alloy C), and 71.0Fe-25.5Cr-2.0Al-0.5Ti (alloy D) synthesized from appropriate elemental powder blends (with $>$ 99.9 wt pct purity and average 30 to 80 μm size) by mechanical alloying in a Retsch PM 400 high energy four-vial planetary ball mill operated at 300 rpm. The milling media comprised 500 mL capacity stainless steel vials and 10 mm diameter stainless steel balls. Cumulative milling duration ran up to 30 to 40 hours with an intermittent interval of 1 hour for every 2 hours of milling. An additional hour of milling was carried out to introduce uniform dispersion of 1.0 wt pct nanometric Y_2O_3 (20 to 30 nm) in the mechanically alloyed powder mass.

All milling operations were conducted with a ball to powder weight ratio of 10:1 and in wet (toluene) medium to prevent agglomeration and oxidation of powders and to facilitate easy retrieval of milled powders. Sintering of milled powders was carried out at 1000 °C by competitive consolidation methods of hot isostatic pressing,[11,12] high pressure sintering,[13] hydrostatic extrusion[14] and pulse plasma sintering,[15] respectively. The synthesis and consolidation details of the present alloys were reported elsewhere by Karak *et al.*[11–15] For comparison, samples of 17 to 4 PH stainless steel (73.0-Fe-17.5Cr-4.0Cu-4.5Ni-0.4Mn-0.25-Si-0.30Nb-0.04C) with similar geometry and dimension were subjected to identical routine of isothermal oxidation so as to study the relative merits of the present alloys with regard to oxidation resistance vis-à-vis standard martensitic stainless steel used for such elevated temperature application.

Sintering yielded solid discs of 10 mm in diameter and 3.5 to 4.5 mm in height, which were mechanically polished using emery papers and diamond impregnated polishing wheels before usual microstructural investigation and isothermal oxidation studies. For the latter, the dimensions and precise weight were measured before and after various stages of isothermal oxidation studies conducted at 700 °C, 800 °C, and 900 °C inside a 5 cm diameter vertical (quartz tube) furnace with SiC heating elements for a cumulative duration of up to 50 hours. The samples, tied to a platinum wire were suspended to position them within the hot zone of the tube furnace with the other end of the wire hooked to the weighing pan of a very sensitive digital balance with a precision of 0.1 mg. Approximately a gap of 0.15 to 0.20 m was maintained between the steel support-frame and the quartz tube. Such an arrangement allowed continuous or sequential monitoring of extent of oxidation with time at different isothermal temperatures using a Pt-Pt/Rh thermocouple kept in close proximity to the sample. After oxidation, the microstructure, micro-composition and phase aggregate both on the top surface and cross-sectional plane across the oxide scale were carefully examined using field emission gun assisted scanning electron microscope (FESEM), energy dispersive spectroscopy (EDS) and X-ray diffraction (XRD), respectively. The kinetics of oxidation were calculated both from mass gain per unit area with time, and from variation of the thickness of oxide scale formed with time and isothermal temperature of oxidation. Finally, the mechanism of oxidation was investigated through correlation between composition and thickness of the oxidized layer and kinetics of oxidation.

III. RESULTS AND DISCUSSION

Figures 1(a) through (d) reveal the scanning electron (secondary electron) image of the four alloys (Alloys A, B, C, D) after sintering for 1 hour by hot isostatic pressing at 1000 °C, respectively. The microstructure of alloy D is much finer than that of alloy A. As alloy D contains the maximum amount of chromium (25.5 wt pct) among all the alloys subjected to identical processing history, it appears that the extent of grain refinement in sintered product is mainly influenced by the chromium content in the alloy. Similar observation on dependence of grain refinement on chromium content in ferritic alloys was earlier reported by Matijasevic and Almazouzi.[16] Careful study of the subsequently obtained XRD profiles of all the sintered alloys suggests that α-Fe(Cr) (body centered cubic, BCC) phase is the main or matrix phase with small and varying volume fraction of mixed intermetallic ($Fe_{11}TiY$ and $Al_{9.22}Cr_{2.78}Y$) and oxide phase ($Y_2Ti_2O_7$) formed during sintering at 1000 °C. As already mentioned, a detailed discussion on microstructural evolution and mechanical properties of the same set of alloys sintered by four complementary techniques was reported elsewhere by Karak *et al.*[11–15]

Figure 2 displays the isothermal oxidation kinetics of alloy D, synthesized by mechanical alloying and sintering by competing techniques (hot isostatic pressing, high pressure sintering, hydrostatic extrusion and pulse plasma sintering) and expressed as cumulative mass gain (per unit area) as a function of time (t) during isothermal exposure to 900 °C in dry air. As per Figure 2, sintering by hot isostatic pressing lends the highest oxidation resistance in alloy D as compared to

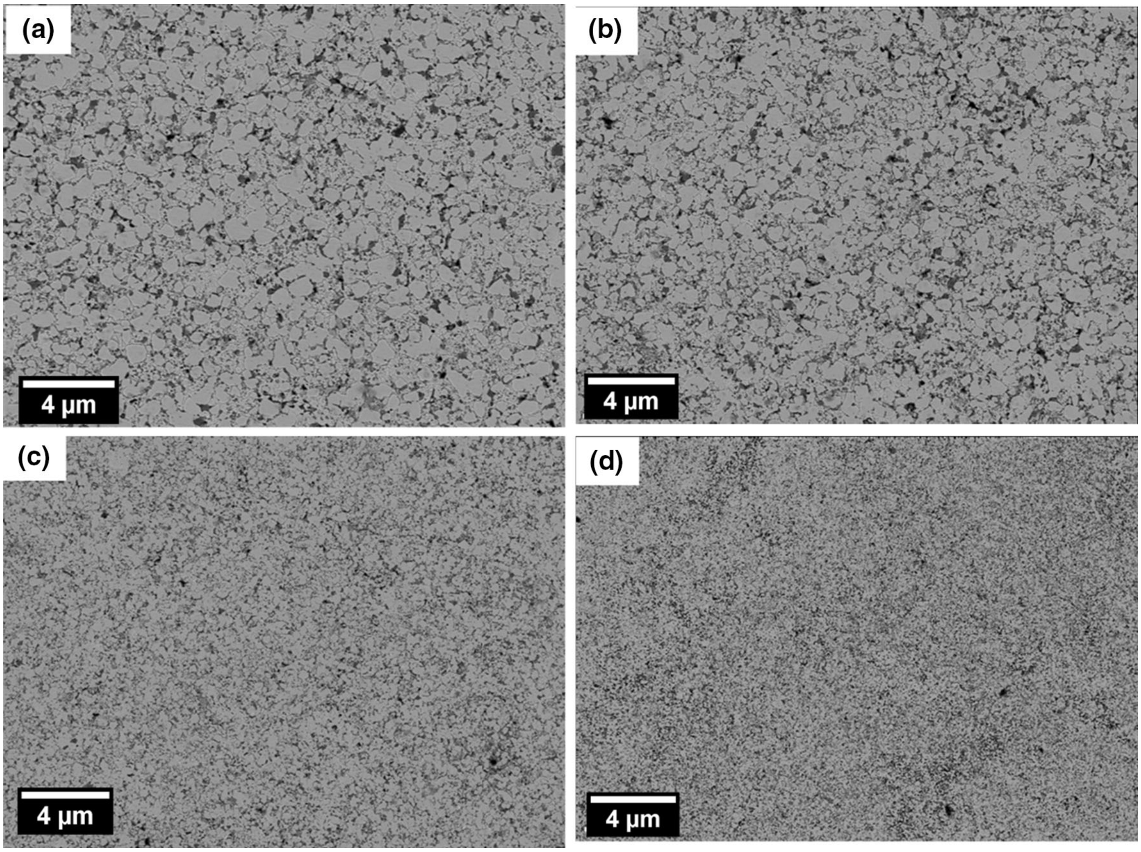

Fig. 1—Scanning electron micrographs of (*a*) alloy A, (*b*) alloy B, (*c*) alloy C and (*d*) alloy D following identical routine of mechanical alloying and sintering by hot isostatic pressing at 1000 °C.

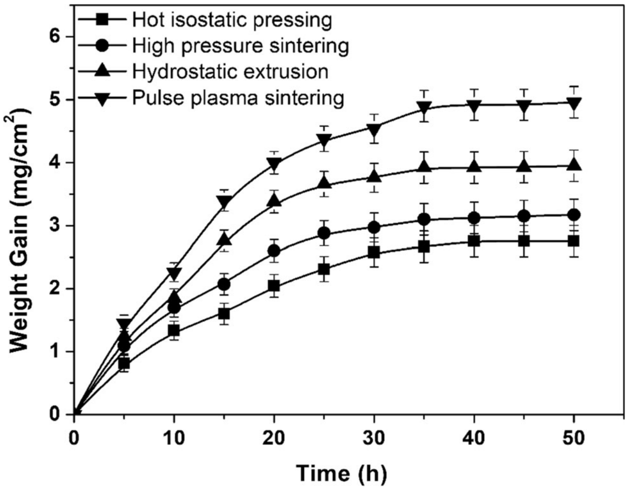

Fig. 2—Kinetics of isothermal oxidation in terms of mass gain per unit area as a function of time during isothermal exposure to 900 °C in dry air for alloy D consolidated by four different techniques: hot isostatic pressing, high pressure sintering, hydrostatic extrusion and pulse plasma sintering.

that measured in samples consolidated by three other techniques. This superior oxidation resistance can be indirectly attributed to better physical (density) and mechanical properties (hardness, elastic modulus and compressive strength) and integrity of the samples sintered by hot isostatic pressing than that by other methods.[11,12] The greater the density, the lower the porosity, and hence, the smaller the chances of oxygen ingress from atmosphere or diffusion from within (internal oxidation). Similarly, higher density reflects greater structural integrity and hence higher mechanical strength and toughness in a sintered product so that internal stresses due to external/internal oxidation and related phase changes could be absorbed and failure from cracks or defects on the surface or inside the bulk could be resisted to a larger extent.

The physical properties (density, porosity) of all the alloys consolidated at 1000 °C by above mentioned techniques are summarized in Table I, which clearly confirms the earlier intuitive inference that method of sintering has a direct bearing on the physical density or porosity of the sintered alloys. The density of alloy A varied from 7.28 to 7.39 g/cm^3, alloy B from 7.23 to 7.34 g/cm^3, alloy C from 7.22 to 7.29 g/cm^3 and alloy D from 7.17 to 7.24 g/cm^3 for different conditions of processing. Furthermore, Table I reveals that among all the techniques explored, hot isostatic pressing offered the maximum density and minimum porosity in all the alloys.

Table I. Summary of Density and Porosity of Samples Consolidated by Different Sintering Techniques at 1000 °C

			Alloy			
Sintering Temperature	Processing Route	Physical Properties	A	B	C	D
1000 °C	hot isostatic pressing	density (g/cm^3)	7.39	7.32	7.29	7.24
		porosity (pct)	0.39	0.35	0.25	0.12
	high pressure sintering	density (g/cm^3)	7.34	7.31	7.28	7.23
		porosity (pct)	0.48	0.39	0.21	0.15
	hydrostatic extrusion	density (g/cm^3)	7.28	7.34	7.29	7.23
		porosity (pct)	0.81	0.77	0.72	0.55
	pulse plasma sintering	density (g/cm^3)	7.39	7.23	7.22	7.17
		porosity (pct)	1.05	0.83	0.75	0.65

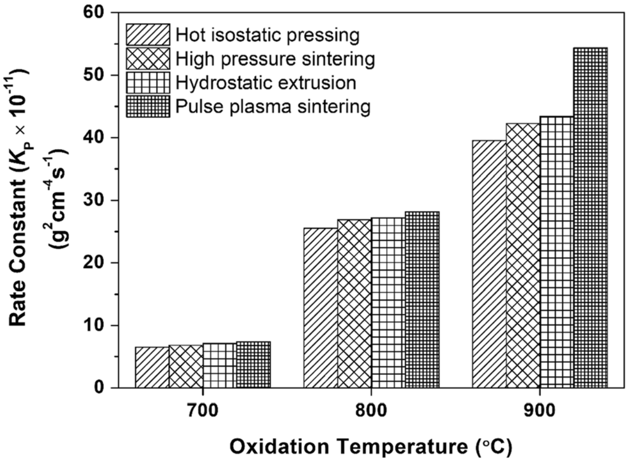

Fig. 3—Rate constants of isothermal oxidation kinetics carried out at 700 °C, 800 °C and 900 °C for up to 50 h in dry air for alloy D consolidated by four different techniques, namely: hot isostatic pressing, high pressure sintering, hydrostatic extrusion and pulse plasma sintering.

Oxidation is both a time and temperature dependent process that is associated with mass gain (unless the reaction product or oxide scale spalls off). Typically, the kinetics of isothermal oxidation follows a parabolic relation as:

$$(\Delta W)^n = K_p t \qquad [1]$$

where, ΔW is mass gain per unit area (mg/cm^2), t is time (h), n is an exponent (with a typical value of 2) and K_p is the rate constant.

Figure 3 compares the rate constant of oxidation (K_p) for isothermal oxidation of alloy D sintered by hot isostatic pressing, high pressure sintering, hydrostatic extrusion and pulse plasma sintering at 1000 °C followed by isothermal oxidation at 700 °C, 800 °C and 900 °C, respectively. It is quite apparent that the rate constant and hence overall kinetics of oxidation increases with increase in isothermal temperature, which is expected as oxidation is a thermally activated and diffusion controlled process. Furthermore, the rate constant is the minimum for all the samples developed by hot isostatic pressing for all temperatures of oxidation. In all the three isothermal conditions, the rate of mass gain is very fast in the initial stage which subsequently slows down and reaches a steady state beyond a certain period of time. Similar trends were observed in all the four alloys.

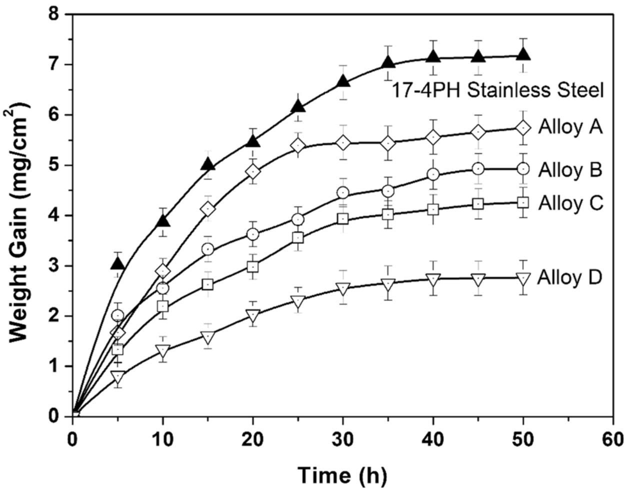

Fig. 4—Kinetics of isothermal oxidation at 900 °C in terms of mass gain per unit area as a function of time for alloy A, alloy B, alloy C and alloy D developed by mechanical alloying and hot isostatic pressing. Data from 17 to 4 PH stainless steel subjected to identical oxidation routine is shown for comparison.

Figure 4 presents the kinetics of isothermal oxidation of the four alloys developed by hot isostatic pressing and compares them with that of 17 to 4 PH stainless steel in air oxidized at 900 °C for periods of up to 50 hours. It appears that the initial rate of oxidation is much faster than the later part (say, beyond 25 hours) indicating perhaps, a protective layer gradually develops on the top surface that retards the scale growth subsequently. Under steady state, the kinetics of oxidation follows the parabolic rate law. Furthermore, the materials loss due to high temperature oxidation is the minimum for alloy D and maximum for alloy A. This behavior seems directly related to the amount of chromium content in the respective alloys as alloy D contains the highest amount of chromium (25.5 wt pct), which is the principal alloying element responsible for protection against oxidation (compared to aluminum or titanium). The rate of oxidation of 17 to 4 PH stainless steel is higher than that of all the four alloys. The current alloys have initially finer grain structure with uniform dispersion of yttria, which has a beneficial effect on creep resistance of metallic alloys used at elevated temperature. It is known that elemental yttrium segregates along boundaries and improves scale adherence and oxidation resistance of ODS alloys.[9,10] However, yttrium has been added in the present alloys as yttria, an oxide compound (Y_2O_3) and not as elemental yttrium, which is the general strategy for all ODS alloys so as to mainly arrest boundary sliding or rupture at elevated temperature and improve creep strength and not necessarily oxidation resistance. Since yttria, having a density (5.01 $\mathrm{g/cm^3}$) much lower than that of iron (7.87 $\mathrm{g/cm^3}$), is usually added in small (0.5 to 1.0 wt pct) quantity in ODS alloys, mechanical alloying followed by sintering is considered more appropriate and effective than conventional melting and casting route to ensure uniform distribution.

Figure 5(a) shows the variation of parabolic rate constant (K_p) of isothermal oxidation as a function of inverse of temperature (T) for all the four alloys investigated in the present study developed by hot isostatic pressing. The activation energy (or temperature coefficient) of isothermal oxidation has been determined from the slope of the straight lines in Figure 5(a) as oxidation is a diffusion controlled process known to follow Arrhenius relationship.[17]

It may be noted that Table II summarizes the activation energy values derived from Figure 5(a) for all the four alloys subjected to isothermal oxidation between 700 °C and 900 °C. Table II indicates that the activation energy of isothermal oxidation is directly related to Cr content of the alloys, *i.e.*, higher the Cr content, greater the activation energy of oxidation. In fact, Figure 5(b) confirms that the average activation energy values, computed from the range or values stated in Table II for all the alloys sintered by various techniques, indeed follow a linear relationship with the chromium content in the temperature range studied. Accordingly, alloy D registers the highest oxidation resistance among all the alloys.

The growth morphology of the oxide scale developed in all the alloys (A, B, C, D) after exposure to 900°C in air for a cumulative duration of 50 hours is shown in Figures 6(a) through (d). It is apparent that the exposed surface is covered with a fairly compact oxide scale with tendency of varying degree of faceting and average crystallite size within about 1 μm in diameter/diagonal. A close comparison reveals that the oxide scale is relatively irregular, rough or even porous for Alloys A, B and C (Figures 6(a) through (c)) possibly due to excess stress generated in the oxide scale arising out of the mismatch of coefficient of thermal expansion between the surface oxides and underlying metallic bulk. Some degree of spallation of scale cannot be ruled out in these cases. In contrast, Figure 6(d) reveals that the surface morphology of the oxide scale in alloy D is more compact, uniform and adherent to the underlying bulk. To establish the utility of the present set of alloys, an identical sample of 17 to 4 PH stainless steel was given the same isothermal oxidation treatment (50 hours at 900 °C in air). Figure 6(e) suggests that surface microstructure of the oxide scale on this 17 to 4 PH stainless steel sample is coarser and more faceted with the individual grain size of approximately 1 to 2 μm and is relatively thicker and porous. Here the difference in morphology of the oxide scale between the present alloys A, B, C, D and that of 17 to 4 PH stainless steel can be attributed to the difference in composition, prior history of processing and hence, interfacial energy of the growth fronts of the oxidized layer on top of these samples. It may be pointed out that defects (porosity, crack) and surface energy play more crucial role in influencing oxidation than morphology (faceted or rough) of the interface.

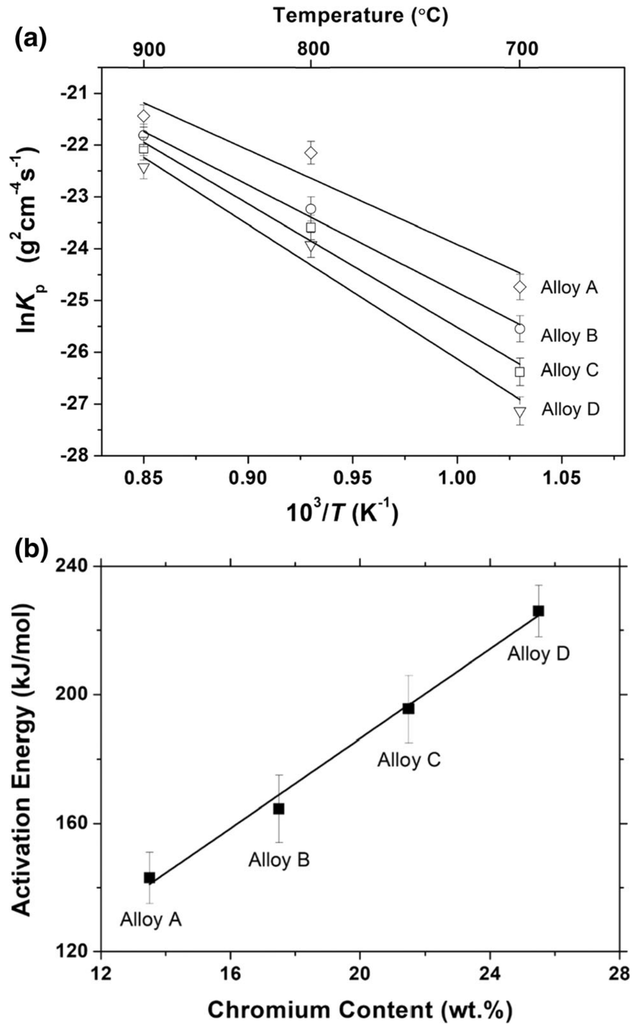

Fig. 5—(*a*) Arrhenius plots for isothermal oxidation at 700 °C, 800 °C, and 900 °C for alloy A, alloy B, alloy C and alloy D consolidated by hot isostatic pressing at 1000 °C, and (*b*) variation of average activation energy for oxidation in the range 700 °C to 900 °C as a function of nominal chromium content in alloys A, B, C and D (with constant quantity of Al, Ti and Y_2O_3) consolidated by various techniques (data from Table II).

Figures 7(a) through (c) show the cross-sectional view of the oxide scales of alloy D developed by hot isostatic

Table II. Summary of Arrhenius Parameters Related to Isothermal Oxidation of the Present Alloys Consolidated by Four Different Sintering Techniques

Processing Routes	Alloy	Oxidation Temperature (°C)	Rate Constant ($g^2cm^{-4}s^{-1}$) ($K_p \times 10^{-11}$)	Activation Energy (kJ/mol)
Hot Isostatic Pressing	A	700	6.5	151
		800	25.5	
		900	39.6	
	B	700	1.07	175
		800	10.5	
		900	26.8	
	C	700	0.34	206
		800	5.5	
		900	25.7	
	D	700	0.19	234
		800	3.9	
		900	22.0	
High Pressure Sintering	A	700	6.87	146
		800	26.8	
		900	42.3	
	B	700	1.65	168
		800	12.7	
		900	29.5	
	C	700	1.05	185
		800	8.4	
		900	26.1	
	D	700	0.56	228
		800	5.8	
		900	24.6	
Hydrostatic Extrusion	A	700	6.92	135
		800	27.2	
		900	43.4	
	B	700	1.75	154
		800	12.5	
		900	29.2	
	C	700	1.15	185
		800	8.8	
		900	26.8	
	D	700	0.43	218
		800	6.1	
		900	25.4	
Pulse Plasma Sintering	A	700	7.34	136
		800	28.1	
		900	54.2	
	B	700	2.82	172
		800	14.5	
		900	33.5	
	C	700	1.74	189
		800	10.5	
		900	28.2	
	D	700	1.02	224
		800	7.56	
		900	26.3	

pressing (at 1000 °C) in the temperatures range 700 to 900 °C for a cumulative oxidation period of 50 hours. It is observed that the scales are protective and uniform in thickness growing toward the outer direction of the surface. Furthermore, the oxide scale thickness increases with increase in temperature. Hence, from Figure 7 it may be concluded that oxide scale forms by the outward diffusion of cations having higher affinity for oxygen from the interior/bulk toward the scale-air interface.

It has been proposed that oxidation of ODS alloys at the initial stage proceeds by internal oxidation involving formation of discontinuous Cr_2O_3 layer.[18–23] In case of lower Cr containing alloy (alloy A), it is anticipated that a very thin layer of α-Fe_2O_3 or Fe-rich α-Fe_2O_3–Cr_2O_3 covers the main oxide scale consisting of Fe_3O_4 merging into the top layer of Fe + $Fe_{(2-x)}Cr_xO_4$ (richer in chromium) near the external surface. It is known that iron-rich oxides thicken preferentially on grains and

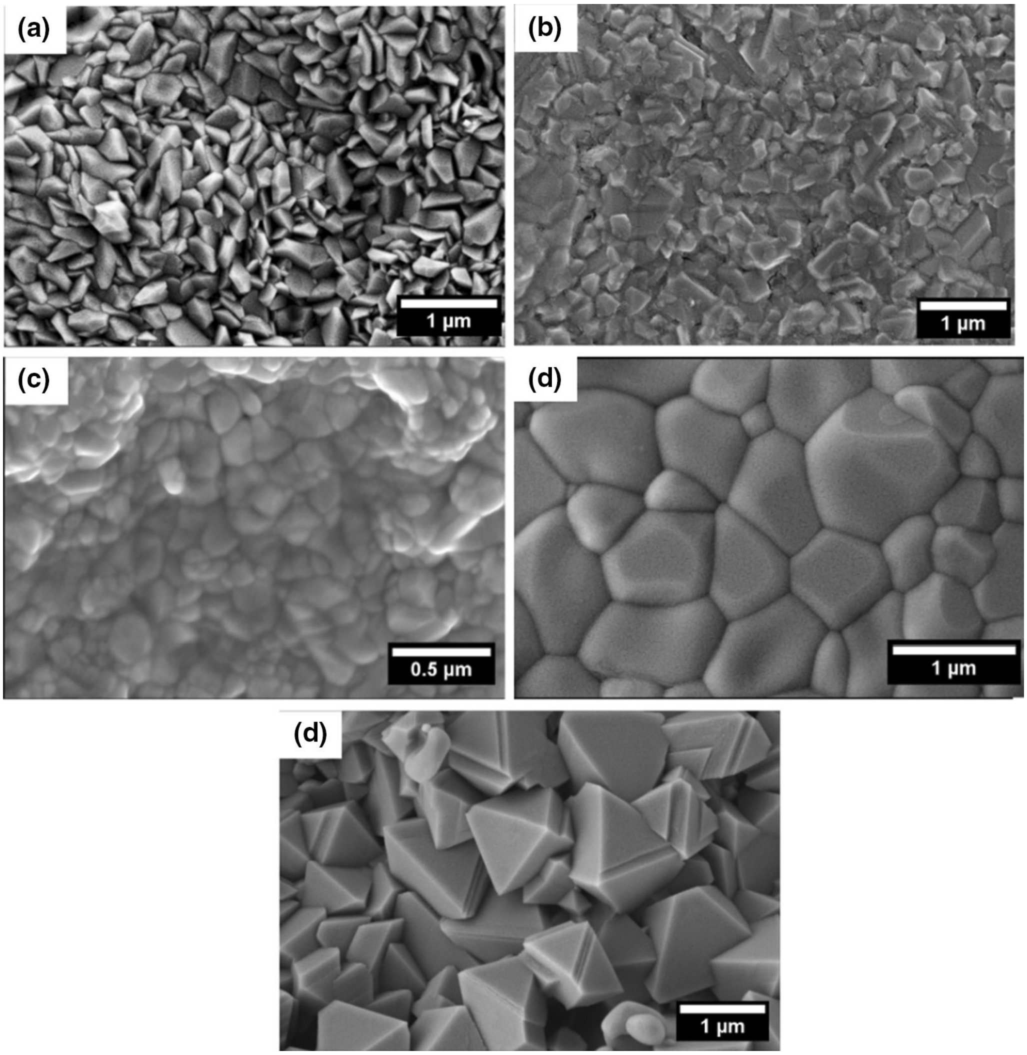

Fig. 6—FESEM images of the top surface of samples following isothermal oxidation at 900 °C for 50 h for (*a*) alloy A, (*b*) alloy B, (*c*) alloy C and (*d*) alloy D (all consolidated by hot isostatic pressing) and (*e*) commercial 17 to 4 PH stainless steel (for comparison).

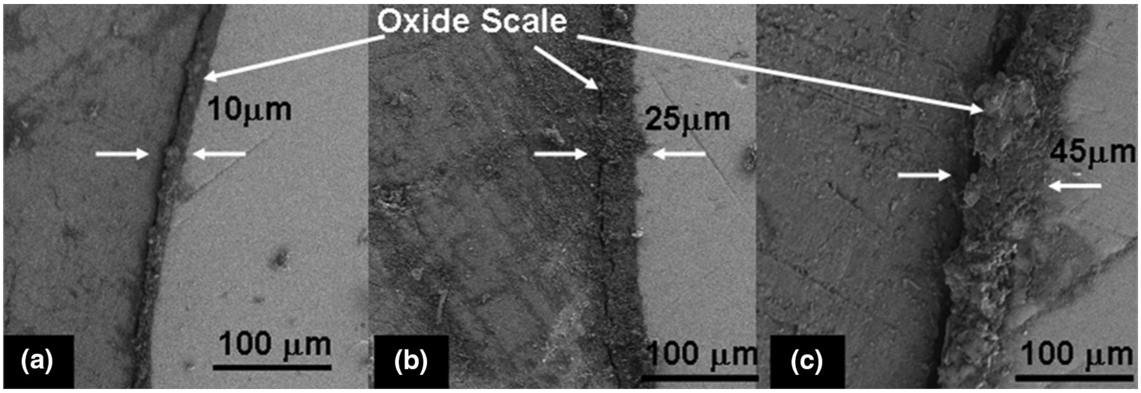

Fig. 7—FESEM images of the cross-sectional growth of the oxide scale in alloy D consolidated by hot isostatic pressing during isothermal and isochronal (50 h) oxidation at (*a*) 700 °C, (*b*) 800 °C and (*c*) 900 °C, respectively.

particularly in the vicinity of dislocation forests, sub-grains, and grain boundaries, which are higher energy sites due to higher defect density in a crystalline aggregate.[21] These defects including boundaries are known to provide local paths of easy diffusion in the oxide layer depending on the structure and orientation

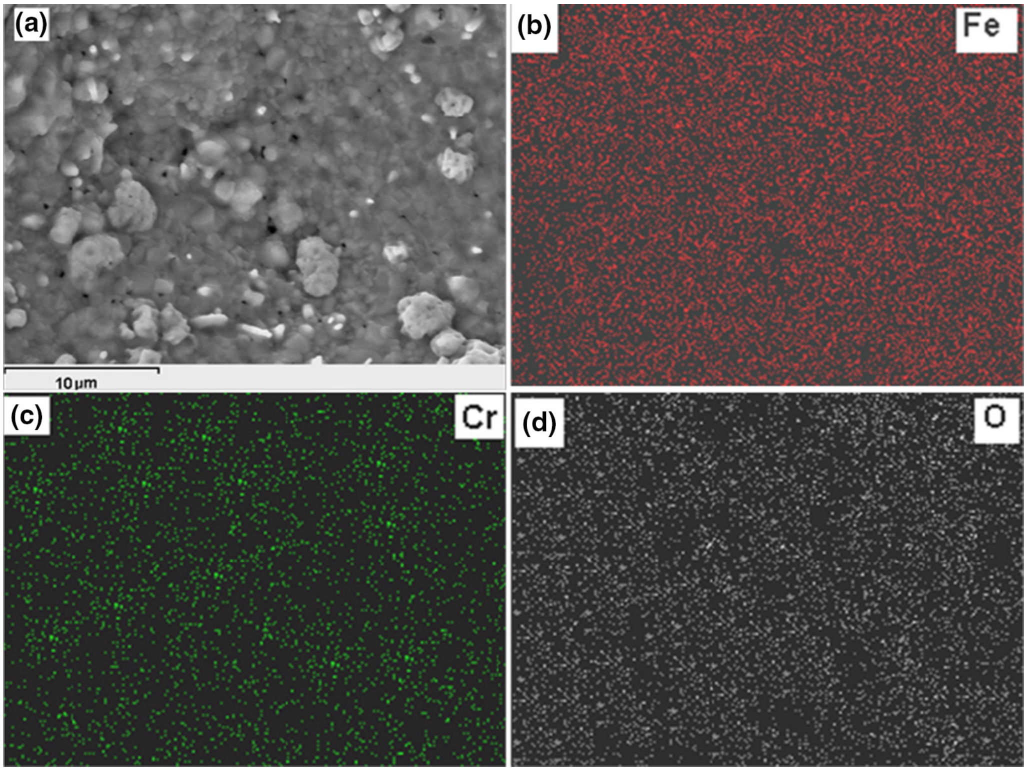

Fig. 8—(*a*) Surface morphology (at low magnification) of the top surface of alloy D (consolidated by hot isostatic pressing) following isothermal oxidation at 900 °C for 25 h showing typical oxide growth features and some porosity. Corresponding elemental distribution of iron, chromium and oxygen measured by X-ray mapping is recorded in (*b*), (*c*) and (*d*), respectively.

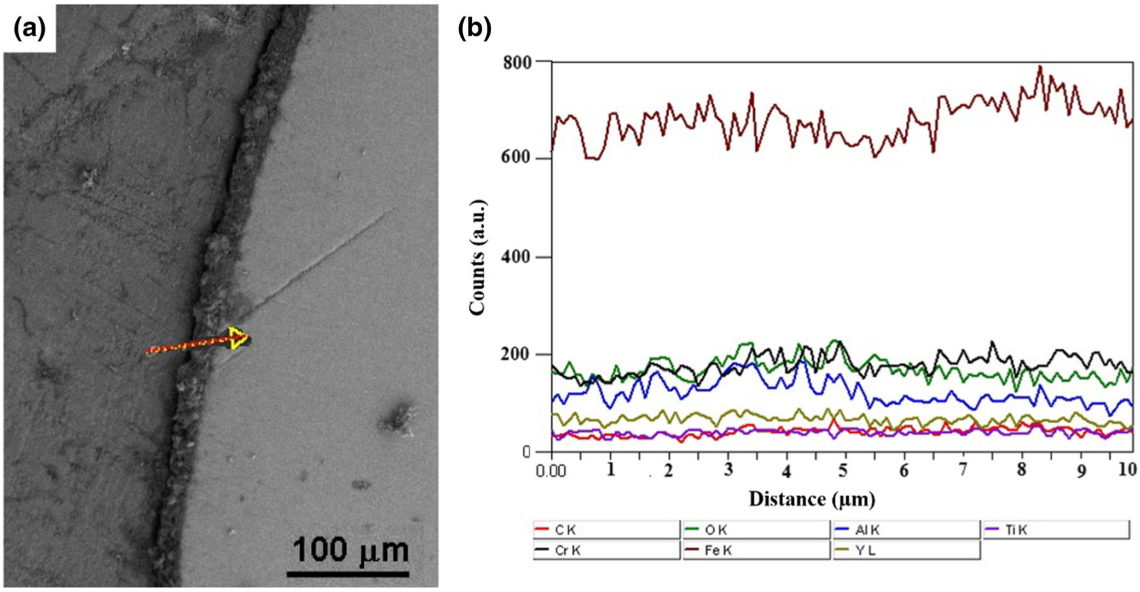

Fig. 9—(*a*) Scanning electron micrograph of the cross section of alloy D following hot isostatic pressing at 1000 °C and isothermal oxidation at 700 °C for 50 h and (*b*) line profile analysis showing the distribution of different elements.

of the crystallites in this layer.[19,20] Furthermore, Fe^{+2} or Fe^{+3} ions are likely to migrate toward the free surface leading to the formation and rapid growth of Fe_2O_3 (or mixed oxides of Fe). If an intervening Cr_2O_3 phase impedes ionic transport of Fe^{+2} or Fe^{+3}, Fe_2O_3 could still nucleate and grow discontinuously in areas such as the non-compact Cr_2O_3 scale, pores or other micro-defects in this region leading to volumetric expansion and even formation of voids and cracks.[18–23] Subsequently, it is expected that outward diffusion of Cr

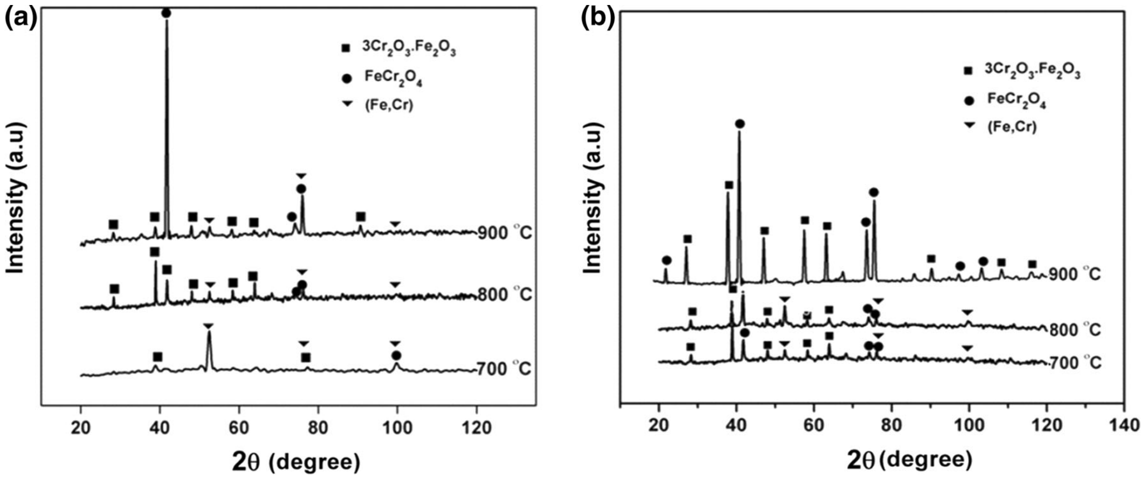

Fig. 10—XRD patterns of (*a*) alloy A and (*b*) alloy D, both consolidated by hot isostatic pressing at 1000 °C and subjected to isothermal oxidation at different temperatures.

ion into Fe$_2$O$_3$ scale in course of extended period of exposure at this temperature range (700 °C to 900 °C) may lead to dissolution of Cr^{3+} in Fe$_2$O$_3$ lattice (cationic sub-lattice) to form 3Cr$_2$O$_3$·Fe$_2$O$_3$ and FeCr$_2$O$_4$ mixed oxide scales. This Cr diffusion and dissolution not only could cause formation of stable 3Cr$_2$O$_3$·Fe$_2$O$_3$ phase, it may also fill the gaps/pores within Cr$_2$O$_3$-rich scales in areas without Fe$_2$O$_3$ and stop the inward diffusion of oxygen to restrict the formation or continuous growth of the oxide scale. Thus the chemical reactions associated with the formation of oxide scale layer in the range 700 °C to 900 °C may be summarized as:

$$4\mathrm{Cr} + 3\mathrm{O}_2 \rightarrow 2\mathrm{Cr}_2\mathrm{O}_3 \quad [2]$$

$$4\mathrm{Fe} + 3\mathrm{O}_2 \rightarrow 2\mathrm{Fe}_2\mathrm{O}_3 \quad [3]$$

$$\mathrm{Fe}_2\mathrm{O}_3 + 3\mathrm{Cr}_2\mathrm{O}_3 \rightarrow 3\mathrm{Cr}_2\mathrm{O}_3 \cdot \mathrm{Fe}_2\mathrm{O}_3 \quad [4]$$

$$\mathrm{FeO} + \mathrm{Cr}_2\mathrm{O}_3 \rightarrow \mathrm{FeCr}_2\mathrm{O}_4 \quad [5]$$

Figure 8(a) shows the microstructure of a typical oxide scale and Figures 8(b) throuh (d) reveals the corresponding elemental distribution by X-ray mapping on the surface of the oxide scale developed on alloy D sample oxidized at 900 °C for 25 hours. On the whole, Figure 8 indicates that the composition of the oxide scale, even if it is made up of mixed oxides of Fe and Cr, does not vary significantly on the surface. The detailed composition analysis of the oxide scale was also undertaken with depth or thickness across the scale (Figure 9).

Figures 9(a) and (b) show the (a) microstructure of the oxide scale along the cross-sectional plane of alloy D following oxidation at 700 °C for 50 hours and (b) corresponding line profile analysis showing the distribution of different elements along the cross section. A careful scrutiny of Figures 8 and 9 would confirm that variation of composition, if any, is marginal both on the surface and along vertical below the surface. Furthermore, the scale is more likely to be a mixed oxide than comprising two different and separate oxides of Fe and Cr. X-ray diffraction spectra obtained from the oxidized surface of alloy A (Cr lean) and alloy D (Cr rich) following isothermal oxidation in dry air at 700 °C to 900 °C as shown in Figure 10. It may be noted that the oxide layer was already identified as 3Cr$_2$O$_3$.Fe$_2$O$_3$ and FeCr$_2$O$_4$ spinel type oxide on the surface of alloy D. The intensity of the oxide peaks in alloy D is much stronger than that of alloy A. In low Cr containing alloy A, both chromium-rich and iron-rich oxides grow on the surface. On increasing Cr to over 20 wt pct (say, in alloy C or D), Fe^{2+} ions are progressively blocked by the FeCr$_2$O$_4$ islands and FeO layer correspondingly becomes thinner relative to the thickness of the Fe$_3$O$_4$-layer. In this condition, the reaction rate is still quite high, as in case of pure Fe. For alloys with higher Cr content, a scale of mixed oxide spinel 3Cr$_2$O$_3$.Fe$_2$O$_3$ is developed with the corresponding parabolic rate constant getting reduced.

It is well known that growth of oxide scale at elevated temperature on top of a metallic alloy mainly proceeds by counter-ionic diffusion. Since Cr is the main alloying element (13.5 to 25.5 wt pct) in the present alloys with high affinity for oxygen, it is expected that Cr, besides Fe, will be main constituent of the oxide scale in all the four alloys. Indeed Figure 10 shows that the scale comprises two mixed oxides of Fe and Cr (3Cr$_2$O$_3$.Fe$_2$O$_3$ and FeCr$_2$O$_4$) as the main constituents apart from the BCC matrix (Fe,Cr) phase. Furthermore, the ionic radius of Fe^{+3} (78.5 pm) is very close to that of Cr^{3+} (75.5 pm) and widely different than that of Y (104 pm), Al (67.5 pm) or Ti (81 pm) in similar valence states. Thus, results of Figure 10 showing mixed oxides of Cr + Fe as main constituents of the scale is justifiable. However, the activation energy for oxidation (related to diffusion) in the present alloys in the temperature range studied (135 to 234 kJ/mol) is considerably lower than that activation energy for volume diffusion of Cr in

BCC-Fe rich matrix phase (~ 276.4 ± 4.4 kJ/mol) in identical temperature range (885 to 1174 K).[24] This difference can be attributed to the possible contributions of boundary diffusion[19,20] and defect aided diffusion in the oxide scale. It may be pointed out that diffusion during oxidation could be of mixed nature with ionic transport both through the bulk/volume and along grain boundaries, as proposed by Harrison *et al*.[20]

Various oxides of reactive elements like Ti, Al and Zr present in ODS alloys may form during exposure to elevated temperature and influence the kinetics and mechanism of oxidation.[25] The present alloys contain Al and Ti in rather low and fixed amount (2.0 and 0.5 wt pct, respectively). While significant contribution or influence of Al or Ti to oxidation resistance is discounted in the present alloys obviously because of very low concentration of them relative to Fe and Cr, similarly, direct contribution of Y in oxidation protection is ruled out here as Y is present only in the oxide (Y_2O_3) form and not in elemental state. However, previous studies on the same set of alloys have indicated that Y_2O_3 may decompose or dissolve and re-precipitate as one of the possible complex oxides (*e.g*., $Y_2Ti_2O_7$, Fe_2TiY or $Al_{9.22}Cr_{2.78}Y$) either during high energy planetary ball milling or subsequent sintering by hot isostatic pressing,[12] high pressure sintering,[13] hydrostatic extrusion,[14] and pulse plasma sintering[15] at elevated temperature and significantly contribute toward mechanical strengthening. Similar results of formation of various oxides of Ti, Al, Zr or Y were also cited by Oono *et al*.[25] In fact, Klueh *et al*.[26] have explained how such oxides can significantly improve tensile and creep strength of Fe-12Cr-0.25Y_2O_3 and Fe-12Cr-2.5W-0.4Ti-0.25Y_2O_3 (wt pct) ODS alloys. A recent study[27] explains that these precipitates or dispersoids can greatly influence grain boundary sliding during superplastic flow at elevated temperature and evolution of anisotropic microstructure and even dynamic recrystallization that would eventually determine the mechanical properties in ODS alloys.

IV. SUMMARY AND CONCLUSIONS

We have studied the isothermal oxidation behavior of nano-Y_2O_3 dispersed ferritic alloys developed by mechanical alloying and subsequent consolidation by hot isostatic pressing, high pressure sintering, hydrostatic extrusion and pulse plasma sintering and compared the same with that of 17 to 4 PH stainless steel. From our detailed analysis the following inferences may be arrived at:

1. Oxidation resistance property of the present oxide dispersion strengthened (ODS) alloys is significantly better than that of 17 to 4 PH stainless steel.
2. Oxidation of all the samples follow the parabolic kinetics with the rate constant varying with composition and isothermal oxidation temperature.
3. The rate and extent of oxidation decreases as Cr concentration in the alloy increases with the maximum reduction in oxidation rate recorded in alloy D (containing 25.5 wt pct Cr).
4. Samples consolidated by hot isostatic pressing registers the most significant resistance to oxidation as compared to that of the samples consolidated by other three techniques (high pressure sintering, hydrostatic extrusion, pulse plasma sintering).
5. The activation energy of isothermal oxidation in the present alloys ranges from 135 to 234 kJ/mol with the maximum value observed in alloy D.
6. The improvement in oxidation resistance of the present set of nano-Y_2O_3 dispersed ferritic alloys is attributed to the formation of a continuous, defect-free and adherent mixed spinel oxide of Fe and Cr with an average composition of $3Cr_2O_3$. Fe_2O_3 and $FeCr_2O_4$, as confirmed by X-ray diffraction analysis combined with compositional mapping by energy dispersive spectroscopy by X-ray.

ACKNOWLEDGMENTS

The authors gratefully acknowledge the partial financial support for the present study from the Department of Science and Technology (Project JCP and DGL) and from the Indian Space Research Organization (Project NCH and ONC), Government of India.

REFERENCES:

1. R. Viswanathan and W. Bakker: *J. Mater. Eng. Perform*., 2001, vol. 10 (1), pp. 81–95.
2. W. Yan, W. Wang, Y.Y. Shan, and K. Yang: Front*Mater. Sci*., 2013, vol. 7 (1), pp. 1–27.
3. K. Asano, V. Kohno, A. Kohyama, T. Suzuki, and H. Kusanagi: *J. Nucl. Mater*., 1988, vol. 155, pp. 928–34.
4. I. Hilger, X. Boulnat, J. Hoffmann, C. Testani, F. Bergner, Y. De Carlan, F. Ferraro, and A. Ulbricht: *J. Nucl. Mater*., 2016, vol. 472, pp. 206–14.
5. R.L. Klueh, J.P. Shingledecker, R.W. Swindeman, and D.T. Hoelzer: *J. Nucl. Mater*., 2005, vol. 341, pp. 103–14.
6. S. Ohtuska, S. Ukai, M. Fujiwara, T. Kaito, and T. Narita: Mater*Trans. A*, 2005, vol. 46 (3), pp. 487–92.
7. S. Ukai, S. Mizuta, T. Yoshitake, T. Okuda, M. Fujiwara, S. Hagi, and T. Kobayashi: *J. Nucl. Mater*., 2000, vols. 283–87, pp. 702–06.
8. M.K. Miller, D.T. Hoelzer, E.A. Kenik, and K.F. Russell: *Intermetallics*, 2005, vol. 13, pp. 387–92.
9. R.A. Versaci, D. Clemens, W.J. Quadakkers, and R. Hussey: *Sloid State Ionics*, 1993, vol. 59, pp. 235–42.
10. T.A. Ramanarayanan, R. Ayer, R. Petkovic-Luton, and D.P. Leta: *High Temp. High Press*., 1988, vol. 20, pp. 277–92.
11. S.K. Karak, C.S. Vishnu, Z. Witczak, W. Lojkowski, J.D. Majumdar, and I. Manna: *Wear*, 2010, vol. 270, pp. 5–11.
12. S.K. Karak, T. Chudoba, Z. Witczak, W. Lojkowski, and I. Manna: *Mater. Sci. Eng. A*., 2011, vol. 528, pp. 7475–83.
13. S.K. Karak, J.D. Majumdar, Z. Witczak, W. Lojkowski, L. Ciupinski, K.J. Kurzydlowski, and I. Manna: *Metall. Mater. Trans*., 2013, vol. 44A, pp. 2884–94.
14. S.K. Karak, J.D. Majumdar, Z. Witczak, W. Lojkowski, and I. Manna: *Mater. Sci. Eng. A*, 2013, vol. 580, pp. 231–41.
15. S.K. Karak, J.D. Majumdar, W. Lojkowski, A. Michalski, L. Ciupinski, K.J. Kurzydlowski, and I. Manna: *Philos. Mag. A*, 2012, vol. 92, pp. 516–34.

16. M. Matijasevic and A. Almazouzi: *J. Nucl. Mater*., 2008, vol. 377, pp. 147–54.
17. R. Soundberg: *Chemometr. Intell. Lab. Syst*., 1998, vol. 41, pp. 249–52.
18. M. Han, S. Peng, Z. Wang, Z. Yang, and X. Chen: *J. Power Sources*, 2007, vol. 164, pp. 278–83.
19. Y. Mishin, C. Herzig, J. Bernardini, and W. Gust: *Int. Mater. Rev*., 1997, vol. 42, pp. 155–78.
20. L.G. Harrison: *Trans. Faraday Soc*., 1961, vol. 57, pp. 1191–99.
21. B. Chattopadhyay and G.C. Wood: *Oxid. Met*., 1970, vol. 2, pp. 373–98.
22. J.H. Kim, K.M. Kim, T.S. Byun, D.W. Lee, and C.H. Park: *Thermochim. Acta*, 2014, vol. 579, pp. 1–8.
23. Y. Chen, K. Sridharan, T. Allen, and S. Ukai: *J. Nucl. Mater*., 2006, vol. 359, pp. 50–58.
24. Chan.-Gyu. Lee, Yoshiaki. Iijima, Tatsuhiko. Hiratani, and Ken.-ichi. Hirano: Mater*Trans. JIM*, 1990, vol. 31 (4), pp. 255–61.
25. N.H. Oono, S. Ukai, K. Tominaga, N. Ebisawa, and K. Tomura: *J. Mater. Sci*., 2019, vol. 54, pp. 8786–99.
26. R.L. Klueh, P.J. Maziasz, I.S. Kim, L. Heatherly, D.T. Hoelzer, N. Hashimoto, E.A. Kenik, and K. Miyahara: *J. Nucl. Mater*., 2002, vols. 307–311, pp. 773–77.
27. H. Masuda, H. Tobe, E. Sato, Y. Sugino, and S. Ukai: *Acta Mater*., 2017, vol. 132, pp. 245–54.